Nonlinear Dynamics **37:** 207–226, 2004.

Basins of Attraction of Periodic Oscillations in Suspension Bridges

MÁRIO S. T. DE FREITAS[1,2], RICARDO L. VIANA[2,*], AND CELSO GREBOGI[3,4]
[1]*Departamento de Física, Centro Federal de Educação Tecnológica do Paraná, 80230-901 Curitiba, Paraná, Brazil;* [2]*Departamento de Física, Universidade Federal do Paraná, 81531-990 Curitiba, Paraná, Brazil;* [3]*Instituto de Física, Universidade de São Paulo, 05315-970 São Paulo, São Paulo, Brazil;* [4]*Institut für Physik, Universität Potsdam, 14415 Potsdam, Germany;* **Author for correspondence (e-mail: viana@fisica.ufpr.br; fax: +55-41-3613418)*

(Received: 6 October 2003; accepted: 17 May 2004)

Abstract. We consider the dynamics of the lowest order transversal vibration mode of a suspension bridge, for which the hangers are treated as one-sided springs, according to the model of Lazer and McKeena [*SIAM Review* **58**, 1990, 537]. We analyze in particular the multi-stability of periodic attractors and the basin of attraction structure in phase space and its dependence with the model parameters. The parameter values used in numerical simulations have been estimated from a number of bridges built in the United States and in the United Kingdom, thus taking into account realistic, yet sometimes simplified, structural, aerodynamical, and physical considerations.

Key words: basins of attraction, multistability, suspension bridges

1. Introduction

The Tacoma Narrows bridge failure, that occurred in the morning of November 7, 1940, is generally taken as a paradigmatic example of the resonance effects on structures under the action of time-periodic forcing caused by a von Kármán street of staggered vortices due to impinging wind on the bridge structure [1]. Even recognizing that the ultimate source of problem is the interaction between the periodicities of the bridge oscillations and the vortices that are created in the von Kármán street, it turns out that the standard textbook explanation, based on linear resonance arguments, is somewhat imprecise [2]. Linear resonance is a rather narrow phenomenon and very difficult to occur in an irregularly changing environment [3].

The possible inadequacy of a linear explanation for the Tacoma Narrows disaster was already pointed out by the board of experts (including von Kármán himself), that wrote a report to the U.S. Federal Works Agency [1]. Due to advances in the understanding of nonlinear oscillators [4], the role of nonlinear effects in the dynamical behavior of suspension bridges has been better appreciated. In this perspective, two aspects of the Tacoma Narrows bridge failure deserve a particular attention. Firstly, it was originally built with a slender and flexible roadbed, according to architectural principles of lightness and grace to yield an artistic appearance. In part, as a result of this design, large-amplitude transversal oscillations occurred in the Tacoma Narrows bridge under the widely different wind conditions that prevail in that place. The bridge was nicknamed 'Galloping Gertie' by virtue of the amazing oscillations exhibited by its roadbed, even with mild breezes.

Secondly, as can be seen in the famous movie shot at the moment of the disaster, besides vertical modes, torsional oscillations were also observed just before the bridge collapse [3]. Mode coupling is a typical nonlinear feature [4]. Moreover, the torsional mode is particularly sensitive to the nonlinear elasticity of the hangers connecting the roadbed to the main suspension cable. The hangers can be approximated

as one-sided springs, for they strongly resist to stretching but do not to compression, what leads to a piecewise linear stiffness for the cables, if the deformations are small enough to be treated in the elastic limit. Other mechanical systems with such discontinuities are found in vibro-impact problems, like impact oscillations with clearances or gaps between moving parts [5–8].

Although a complete description of the spatio-temporal pattern of the roadbed would need the solution of a boundary value problem for the partial differential equation describing the beam vibrations [9], a simpler description can be given by considering the main vibration modes exhibited by the bridge roadbed. Taking into account the behavior displayed by the Tacoma Narrows bridge just before its failure, the first transversal harmonic was the dominant one and it resulted in a vibration amplitude of 1.5 ft, excited by 35 mph winds. After 3 h, the wind increased to 42 mph and the growing oscillation amplitude caused a hanger to snap from its roadbed connection, resulting in an unbalanced loading and to a 0.2 Hz torsional vibration model, which ultimately caused the bridge to collapse [10]. Hence, in the following, we will concentrate on the dynamics of the lowest transversal vibration mode, whose time evolution is governed by an ordinary differential equation [3]. Doole and Hogan [11] have considered the periodic response of the bridge to variations of the external driving parameters. In a later work, these authors considered the dynamics of the lowest torsional mode [12].

Being a nonlinear system, the equations describing the time evolution of this mode can exhibit a complex behavior, including periodic, quasi-periodic and chaotic behavior [13]. Moreover, for weak dissipation, there is multi-stable behavior, involving both periodic and chaotic attractors, with a highly convoluted basin of attraction structure [14]. The effect of the model parameters on the erosion of the safe basin, or the set of initial conditions which would lead to the ultimate collapse of the bridge, has been considered in a recent paper [15]. In the numerical simulations of the suspension bridge dynamics made so far [3, 11, 12, 14, 15], the set of model parameters which has been used is dictated more for the sake of convenience in illustrating the dynamical features, than properly by the behavior expected for real bridges. This paper, on the other hand, aims to relate the dynamical behaviors, obtained by numerical simulations, to data from real bridges, taking into account physical, structural, and aerodynamical factors to estimate reliable model parameters.

We structured this paper as follows: in Section 2 we present the model for time evolution of the lowest vibrational mode of a suspension bridge. Section 3 is devoted to the relation between the non-dimensional "bare" parameters of the oscillator mode to the physical magnitudes characterizing a suspension bridge: its elasticity, damping, and wind-induced excitation. An estimation of the model parameters using data from real bridges is made in Section 4. Numerical simulations of the dynamical behavior using this new set of parameters is made in Section 5, where we consider in particular the multi-stability and the basin boundary structure. Our conclusions are left to the final section.

2. Suspension Bridge Model

We assume that the roadbed of a suspension bridge is an elastic vibrating beam sustained by hangers, or steel cables attached to a main suspended cable (Figure 1). The elastic beam is hinged on both ends to an anchorage block, and the main cable is supported by towers. We take into account only the elasticity of the roadbed and of the hangers that support it, thus neglecting deflections of the main suspended cable and other structural components.

The longitudinal and transversal coordinates of the vibrating beam are denoted as x and z, respectively, and $u(x, t)$ is the beam deflection along y, assuming positive downward deflections, and ignoring the influence of the transverse coordinate z (Figure 1). The hangers are modelled as one-sided strings, since they do not withstand compression efforts, and oppose a linear restoring force when stretched, provided

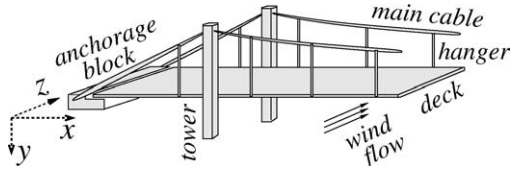

Figure 1. Schematic of a suspension bridge. The hangers connect an elastic beam representing the bridge deck to the main suspension cable.

the deformations are small enough to be treated in the elastic regime [3]. The stiffness of a hanger is piecewise linear and asymmetric, the elastic restoring force being $-k'u^+$, where k' is the spring constant and $u^+ = \max\{u, 0\}$. Hence, the elastic response has two distinct regions: for downward deflections, we take into account the combined response of the beam and stretched hangers, whereas, for upward deflections, only the beam elasticity is considered. A preloading term $W(x)$ is added to account for the proper beam weight and its loading.

The dynamics of the beam vibrations is governed by Equation [16]

$$M\frac{\partial^2 u}{\partial t^2} + EI\frac{\partial^4 u}{\partial x^4} + \delta'\frac{\partial u}{\partial t} = -k'u^+ + W(x) + F(x,t), \tag{1}$$

where M is the beam mass per unit length, E the Young modulus , and I the moment of inertia of its transversal section. The dissipative effect on the beam vibration is modelled by a viscous damping term $\delta' u_t$.

We assume that the wind flows through the roadbed sideways (i.e. along the transversal direction z), such that, if the Reynolds number of the flow is high enough, there is a periodic emission of vortices with a well-defined frequency ω' and spacings, in both horizontal and vertical directions (von Kármán vortex street) [17]. The detachment of the vortices from the obstacle creates a time-periodic external force $F(x,t)$ collinear with the roadbed vertical deflection, and with the same frequency ω':

$$F(x,t) = F_0(x)\sin(\omega' t). \tag{2}$$

The boundary conditions for Equation (1) take into account the hinging of the beam at its ends ($x = 0$ and $x = L$):

$$u(0,t) = u(L,t) = \left.\frac{\partial^2 u}{\partial x^2}\right|_{(0,t)} = \left.\frac{\partial^2 u}{\partial x^2}\right|_{(L,t)} = 0. \tag{3}$$

Rather than trying to solve directly Equation (1), we take the roadbed profile as a superposition of many vertical vibrational modes, each of them with its own dynamics, and satisfying the boundary conditions (3). This would correspond to Fourier-expand $u(x,t)$ such that (1) reduces to a large system of coupled ordinary differential equations. Satisfactory results, however, can be obtained by analyzing only the first (lowest order) vertical mode (Figure 2):

$$u(x,t) = y(t)\sin\left(\frac{\pi x}{L}\right), \tag{4}$$

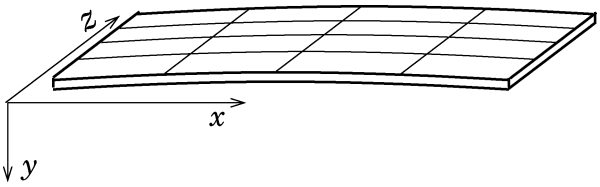

Figure 2. First vertical vibration mode of the beam representing the suspension bridge roadbed.

where $y(t) = u(L/2, t)$ indicates the midpoint deflection, where positive (negative) values stand for downward (upward) deflections. This was actually the most commonly observed mode for low velocities in the Tacoma Narrows bridge before its failure [1]. Moreover, the loss of stability of this mode was responsible for the torsional oscillations that eventually led to the Tacoma Narrows disaster [2].

The influence of higher vibration modes is comparatively weak for low excitation energies, such as those considered in this paper. As far as the torsional modes are concerned, they may be excited by the unbalanced motion caused, for example, by the rupture of a hanger in one of the roadbed sides. This has actually happened in the Tacoma Narrows bridge collapse. This nonlinear effect is thus responsible for the energy transfer between vibrational and torsional modes.

The same assumption (4) implies on choosing only the lowest harmonic for the preload as well as for the spatial part of the external force

$$W(x) = W' \sin\left(\frac{\pi x}{L}\right), \tag{5}$$

$$F_0(x) = B' \sin\left(\frac{\pi x}{L}\right). \tag{6}$$

Since the preloading W is usually taken to be a constant value, the decomposition for $W(x)$, Equation (5), should be intended as the first term in the harmonic expansion of a constant function. The relative error committed in taking only this term is less than 10% [3].

Substituting Equations (4)–(6) into the partial differential equation (1) results in a single ordinary differential equation

$$M\frac{d^2y}{dt^2} + \delta'\frac{dy}{dt} + EI\left(\frac{\pi}{L}\right)^4 y + k'y^+ = W' + B'\sin(\omega' t). \tag{7}$$

Introducing non-dimensional spatial and temporal variables

$$\hat{x} = \frac{\pi x}{L}, \tag{8}$$

$$\hat{t} = \left(\frac{\pi}{L}\right)^2 \sqrt{\frac{EI}{M}}\, t, \tag{9}$$

and the following normalized parameters

$$\delta = \left(\frac{L}{\pi}\right)^2 \frac{\delta'}{2\sqrt{EIM}}, \tag{10}$$

$$k = \left(\frac{L}{\pi}\right)^4 \frac{k'}{EI}, \tag{11}$$

$$\omega = \left(\frac{L}{\pi}\right)^2 \omega' \sqrt{\frac{M}{EI}}, \tag{12}$$

$$B = \left(\frac{L}{\pi}\right)^4 \frac{B'}{EI}, \tag{13}$$

$$W = \left(\frac{L}{\pi}\right)^4 \frac{W'}{EI}, \tag{14}$$

there follows that Equation (7) is rewritten as

$$y'' + 2\delta y' + \ell y = W + B\sin(\omega t), \tag{15}$$

where the primes denote derivatives with respect to the scaled time, the hats on the variables were removed for ease of notation, and the piecewise linear stiffness is represented by

$$\ell = \begin{cases} 1 & \text{if} \quad y < 0, \\ (k+1) & \text{if} \quad y > 0, \end{cases} \tag{16}$$

A mechanical oscillator equivalent to Equation (15) is depicted in Figure 3, where there are two linear springs with stiffnesses equal to 1 and k, respectively. The first spring is always connected to the vibrating mass, whereas the second spring has a fixed clearance. This kind of oscillator has been analyzed mathematically by many authors [18–20] and has many applications in the impact vibration literature [6, 7]. In principle, it would be possible to obtain approximate results by using perturbation methods, such as that of slowly varying amplitude and phase [21]. However, this treatment would be restricted to rather small time intervals, this that only transient behavior would be adequately covered by this approach. On the other hand, we are chiefly concerned with asymptotic behavior, since we are seeking for basins of attractions in the phase space, such that perturbative solutions may not be appropriate to compare with the numerical simulations we have done.

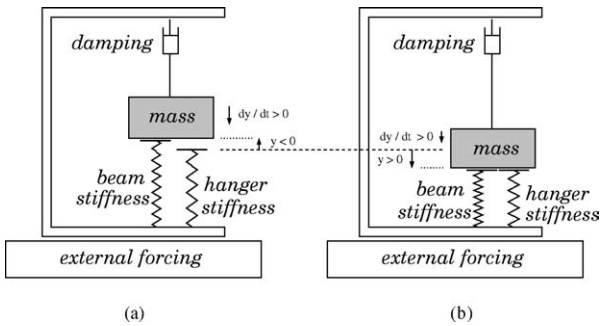

Figure 3. One-dimensional oscillator with two springs, one of them with a clearance, equivalent to the suspension bridge flexional vibrations. (a) Upward deflections, for which only the beam stiffness is acting; (b) downward deflections, for which both the beam and hanger stiffnesses are acting. The string in the upper part of the figure plays no role in the elastic response of the oscillator.

3. Model Parameters for Suspension Bridges

In previous works on this model for vertical oscillations of a suspension bridge [11, 14, 15], parameter values were chosen in an *ad hoc* way, in order to investigate the wide variety of dynamical features present in the model. If we wish to apply these theoretical results to real bridges, it turns to be necessary to use realistic values, which we estimate in this section.

3.1. Elasticity of the Hangers

The bridge roadbed is supposed to be a flexible beam supported by an even number $2N$ of hangers which we treat as one-sided springs. The terms in Equation (1) represent vertical forces *per* unit of length in the longitudinal direction. Hence, the spring constant k', due to the effect of hangers, can be estimated as the quotient between the equivalent elastic constant K of the combination of $2N$ hangers and the roadbed of length L. The elastic constant K refers to a parallel association of springs, each of them with elastic constant K_j, $j = 1, 2, \ldots, N$, corresponding to a pair of hangers.

Each pair of hangers has a different length c_j, determined by the curvature of the main suspension cable, i.e., a function of the longitudinal coordinate x_j (Figure 4). Thus the corresponding elastic constant is $K_j = ES/c_j$, where E is the Young modulus of the hangers (steel) and S the corresponding area of the pair of hangers, which we assume to be the same for all points x_j. Hence, the equivalent elastic constant of the hangers is

$$K = \sum_{j=1}^{N} K_j = \sum_{j=1}^{N} \frac{ES}{c_j}, \tag{17}$$

The shape of the main suspension cable is assumed to be an arch of parabola with arrow $y = -C$ (Figure 4), hence

$$c_j(x_j) = -C\left(\frac{2x_j}{L} - 1\right)^2. \tag{18}$$

The summation in Equation (17) can be replaced by an integral, by assuming that the cross-sectional area of the hangers uniformly distributed along the roadbed, so that the distributed area is (Figure 5):

$$s = \frac{\sum S}{L} = \frac{S(L/e_T)}{L} = \frac{S}{e_T}, \tag{19}$$

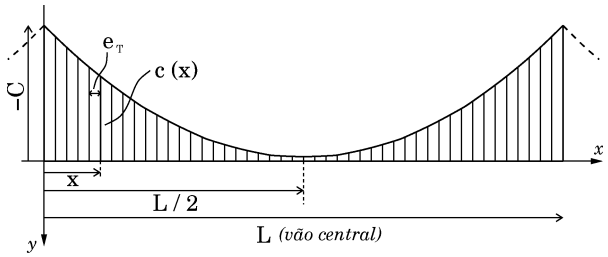

Figure 4. Association of hangers supporting the bridge roadbed.

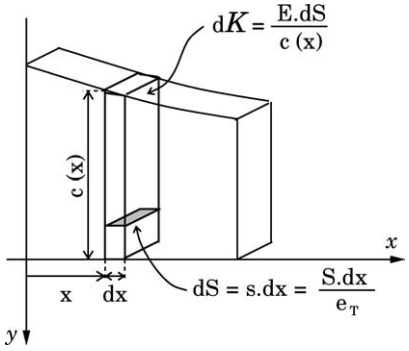

Figure 5. Continuous distribution of hangers.

where $e_{\mathrm{T}} = L/N$ is the spacing between hangers. Hence

$$K = \sum_{j=1}^{L/e_{\mathrm{T}}} K_j \approx \int_{x=0}^{L} \frac{E\,dS}{c(x)}, \tag{20}$$

which, after substituting the parabolic shape (18), results in

$$K = \frac{ESL}{e_{\mathrm{T}}C}, \tag{21}$$

The spring constant is $k' = K/L = ES/e_{\mathrm{T}}C$, whose non-dimensional form is, according to (11),

$$k = \left(\frac{\pi}{L}\right)^{-4} \frac{S}{I e_{\mathrm{T}} C}, \tag{22}$$

I being the beam's moment of inertia.

The preloading term W' in Equation (1) corresponds to the bridge structure weight per unit of roadbed length, and its value is explicitly given in the literature [22].

3.2. Periodic Excitation Due to a von Kármán Vortex Street

As stated in Section 1, the time-periodic external force acting on the suspension bridge is due to a von Kármán vortex street, or the Aeolian Harp effect, extensively studied in the literature [23, 24]. It must be emphasized that other studies have suggested that the Tacoma Narrows Bridge failure would also be influenced by the so-called 'galloping instability', which consists on coupled self-excited bending and torsional excitation [25]. When a fluid flow, with large enough velocity, impinges on an obstacle, it may happen that there is an alternate releasing of vortices by the upper and lower parts of the obstacle (Figure 6), with a well-defined frequency ω', and which causes a time-periodic drag force on the obstacle with direction perpendicular to the flow.

The Reynolds number of the fluid flow is

$$N_{\mathrm{R}} = \frac{DU}{\nu}, \tag{23}$$

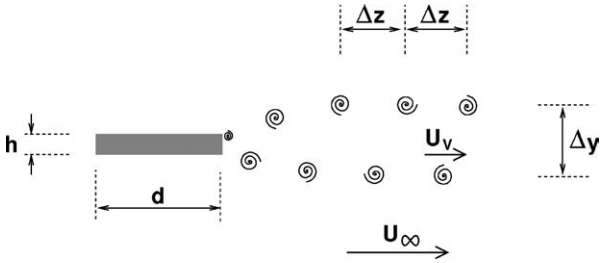

Figure 6. Schematic representation of a von Kármán vortex street on the bridge roadbed.

where D is a characteristic dimension of the obstacle, U is the fluid flow velocity, and ν the kinematic viscosity. The formation of a von Kármán vortex street is expected for the interval $30 < N_{\mathrm{R}} < 120$ [23].

The vortices (two per period) are released with a frequency

$$\omega' = 2\pi \frac{U_{\mathrm{V}}}{\Delta z}, \tag{24}$$

where Δz is the horizontal spacing between the vortices at the bottom (or at the top), Δy being the corresponding vertical spacing, and U_{V} is the velocity of vortex displacement with respect to the obstacle. Notice that ω' is also the frequency of the periodic force on the bridge roadbed.

The roadbed of the suspension bridge can be approximated by a prismatic solid of height h and width d, on a wind-induced fluid flow with velocity U_∞ at infinity. In this case, a standard result states that [23]

$$\omega' = 0.396\pi \left(1 - \frac{19.7}{N_{\mathrm{R}}}\right) \frac{U_\infty}{h}. \tag{25}$$

Considering, what is reasonable, a fluid flow with Reynolds number $N_{\mathrm{R}} = 75$, there results

$$\omega' = 0.230\pi \frac{U_\infty}{h}. \tag{26}$$

The non-dimensional frequency, according to Equation (12), is

$$\omega = 0.230\pi \left(\frac{L}{\pi}\right)^2 \sqrt{\frac{M}{EI}} \frac{U_\infty}{h}, \tag{27}$$

where the mass per unit length can be estimated from the preloading W' and the acceleration of gravity g.

The excitation amplitude B' is the maximum value of the drag force per unit length. The time-averaged value of this force is given by

$$\bar{B}' = \rho U_\infty^2 \Delta y \left[2.83\left(\frac{U_{\mathrm{V}}}{U_\infty}\right) - 1.12\left(\frac{U_{\mathrm{V}}}{U_\infty}\right)^2\right], \tag{28}$$

where ρ is the density of air. Using (25) we can estimate the velocity ratio as

$$\frac{U_{\mathrm{V}}}{U_\infty} = 0.14 \frac{\Delta z}{h}, \tag{29}$$

for a Reynolds number $N_R = 75$. There results

$$B' = \rho U_\infty^2 \Delta y \left[0.396 \left(\frac{\Delta z}{h} \right) - 0.022 \left(\frac{\Delta z}{h} \right)^2 \right]. \tag{30}$$

The non-dimensional amplitude given by Equation (13), turns out to be given by

$$B = \left(\frac{L}{\pi} \right)^4 \frac{1}{EI} \rho U_\infty^2 \Delta y \left[0.396 \left(\frac{\Delta z}{h} \right) - 0.022 \left(\frac{\Delta z}{h} \right)^2 \right]. \tag{31}$$

3.3. Viscous Damping of the Bridge Oscillations

By dimensional analysis of Equation (1), there follows that the coefficient of the damping term corresponds to the ratio between the viscous drag force per unit length and the time derivative of the downward velocity of the roadbed:

$$\delta' = \frac{F_{\text{drag}}/L}{|\partial u/\partial t|} = \frac{b}{L}, \tag{32}$$

where b is a damping coefficient of the corresponding one-dimensional oscillator (see Figure 3).

Assuming oscillations exponentially damped with time, we can write the amplitude of the n-th oscillation cycle, denoted u_n, in terms of the amplitude of the preceding cycle, by the following relation

$$u_{n+1} = u_n e^{\alpha} = u_n \exp\left(- \frac{bT_{\text{N}}}{2m} \right), \tag{33}$$

where $m = ML$ is the total mass of the oscillating system (basically the mass of the roadbed), and T_N is the period of the free (undamped) oscillations. We have also defined the decay constant,

$$\alpha = -\frac{bT_{\text{N}}}{2m} = -\frac{\delta' T_{\text{N}}}{2M}, \tag{34}$$

which applies to suspension bridges [22]. However, it must be noted that the tabulated values (Table 1) refer to experimental results that take into account the *combined* effect of many factors, such as the viscous damping, inelasticity of the structure, friction with the bearings, etc. Hence we can better treat the constant δ' as representing the effect of all forms of damping, with the prevalence of viscous forces.

The non-dimensional damping coefficient, given by (10), is given by

$$\delta = \left(\frac{L}{\pi} \right)^2 \frac{1}{2\sqrt{EI}} . \frac{2\sqrt{M}}{T_{\text{N}}} \alpha \tag{35}$$

4. Specification of Parameter Values for Some Suspension Bridges

In the following, we assume the hangers as made from steel, for which the Young modulus is $E = 2 \times 10^{11}$ N/m^2 (S.I. units are used throughout this paper). Other physical constants are the acceleration of gravity, $g = 9.8$ m/s^2, and the air density $\rho = 1.29$ kg/m^3. The mass per unit length of the bridge is $M = W'/g$. Table 1 presents structural data for some well-known suspension bridges. The last row presents average

Table 1. Structural data for some suspension bridges (adapted from [22]).

Bridge	W' (kN/m)	I (m^4)	L (m)	h (m)	e_T (m)	C (m)
Golden Gate	333	5.28	1280	7.60	15	145
George Washington	584	3.96	1067	9.15	18	96
Forth	153	4.73	1006	8.40	18	91
San Francisco — Oakland	272	8.34	704	9.15	9	70
Verrazano Narrows	535	10.80	1298	7.30	15	117
Original Tacoma Narrows	83	(0.15)	853	2.45	15	71
Average values	327	6.6	1035	7.34	15	98

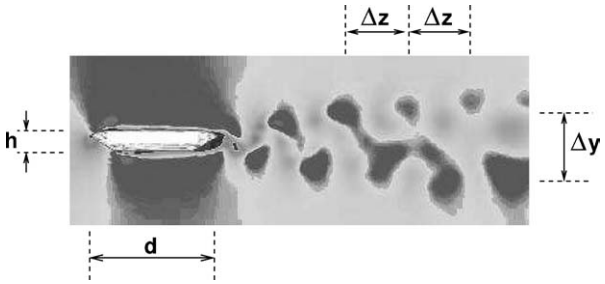

Figure 7. Numerical simulation results for a von Kármán street produced by a prismatic obstacle, obtained by Morgenthal [26].

values for the parameters, to be used in the next sections to guide our numerical simulations of the dynamical system characterizing the bridge oscillations. Note that we have excluded from Table 1 the moment of inertia of the original Tacoma Narrows bridge (before its failure), since it is atypically low (45 times less than the average of the other bridges in the table). In fact, one of the reasons for the ultimate disaster with the Tacoma Narrows bridge was its slender design. After the collapse, the Tacoma bridge was rebuilt and got a more robust roadbed, with a higher moment of inertia.

Not all model parameters are readily found in the literature , and they have to be estimated from indirect measures. For example, the cross-section area of a pair of hangers was estimated as $S = 21.3$ cm^2 in [22], and we take this value for the numerical simulations. The vertical and horizontal spacings between vortices in the von Kármán street have been estimated through results obtained in numerical simulations of the fluid flow by Morgenthal [26], one of his plates being reproduced in Figure 7:

$$\Delta y \approx 3h, \quad \Delta z \approx 2h, \tag{36}$$

where h is the roadbed height (Figure 6). For an average value of $h \approx 15\,m$ (Table 1) there results $\Delta y \approx 22\,m$ and $\Delta z \approx 15\,m$.

An average wind flow velocity of $U_\infty = 20\,\text{m/s} = 72$ km/h is compatible with the Reynolds number (75) we have assumed. However, it must be emphasized that, in realistic situations, the velocity of the wind flow may vary over quite a wide range. For the first flexional asymmetric vibration mode, the natural frequency of oscillations for a typical suspension bridge is about 6.8 min^{-1} [22]. Hence, we estimate the natural frequency of the lowest symmetric vibrational mode as half of this value, or $\omega_N = 2\pi f_N \approx 5 \times 10^{-2}$ rad/s. The constant of logarithmic decay, Equation (34), can be estimated as $\alpha \approx 0.06$.

Table 2 presents parameter values to be used in the numerical simulations made using our theoretical model, and based on the average values for real bridges found in Table 1. We present the original

Table 2. Parameter values to be used in numerical simulations of suspension bridge dynamics.

Parameter	k	W	ω	B	δ
S.I. units	272.1×10^3	327.0×10^3	1.98	8.0×10^3	226.9
Non-dimensionalized	2433.4	2924.3	34.2	71.6	0.117
Order of magnitude	10^3	10^3	10^1	10^2	10^{-1}

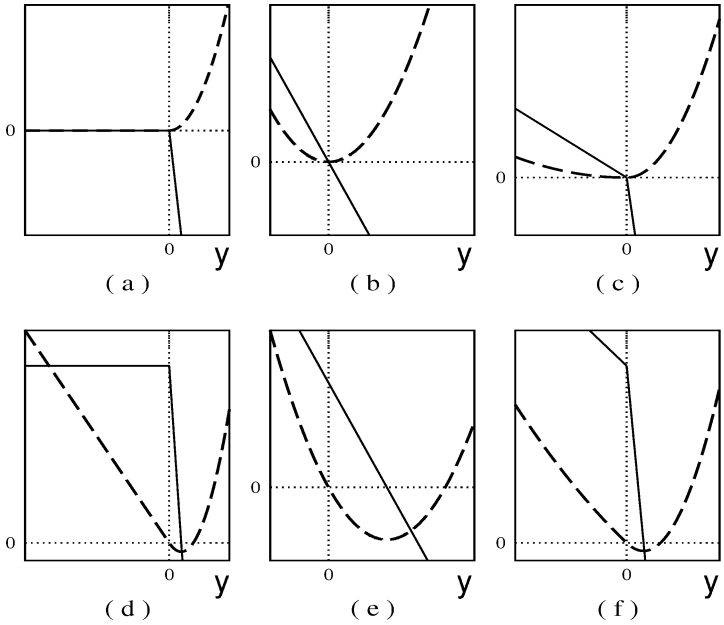

Figure 8. Restoring force (solid line) and the corresponding effective potential (dashed line) as a function of the vertical bridge deflection y, without preload: (a) hanger stiffness; (b) beam stiffness; (c) combined stiffness; (d)–(f): the same cases, but with preload.

parameter values, in S.I. units, their non-dimensionalized values, and respective orders of magnitude.

5. Nonlinear Dynamics of the Suspension Bridge

Let us first consider that both the damping and the external force vanish ($\delta = 0$, $B = 0$). In this case the suspension bridge model (15), governing the deflections of the first vertical vibrational mode, can be written in the form $y'' = F_{\text{eff}}(y) = -dV_{\text{eff}}(y)/dy$, where

$$V_{\text{eff}}(y) = -Wy + \frac{1}{2}my^2 \tag{37}$$

is an effective potential which contains the effects of the piecewise-linear stiffness and the constant preload.

Figures 8a–c show both the effective force and potential for the hangers, beam and the combined system, respectively, without preload ($W = 0$). The hangers act as one-sided springs, according to Equation (8), whereas the beam experiences a linear restoring force, such that the effective potential for

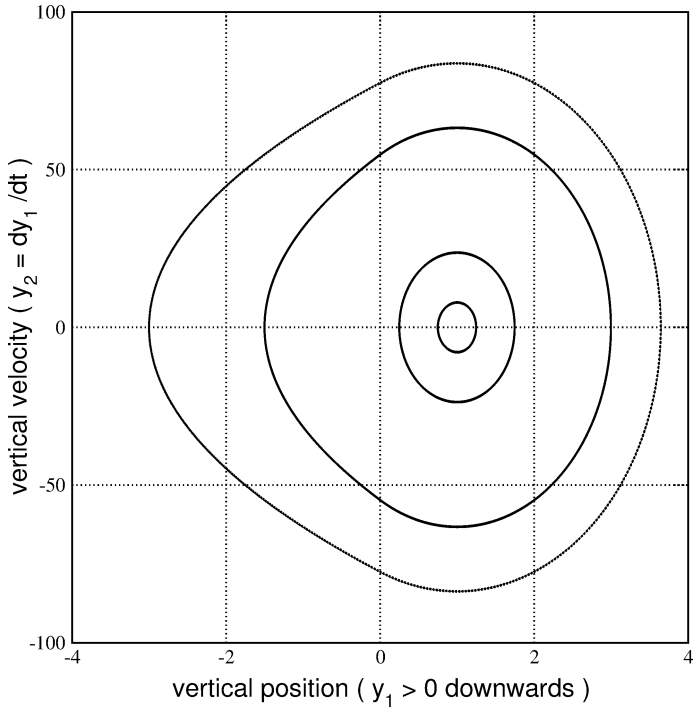

Figure 9. Trajectories in the phase plane ($y_1 = y$, $y_2 = \dot{y}$) for the undamped and free bridge oscillations, with $k = 1000$ and $W = 1000$, corresponding to six different initial conditions. Preloaded orbits have all their points with $y > 0$.

the combined system is an asymmetric curve. The existence of a preload ($W \neq 0$) causes the appearance of a small harmonic well in the bottom of the effective potential curve, as can be seen in Figures 8d–f. Small amplitude oscillations, or preloaded orbits, are strictly linear and can be analytically solved [11]. We are, however, interested in the large amplitude oscillations, for which the non-smoothness of the effective potential plays a key role, and which requires a numerical solution of Equation (15), what has been accomplished with the help of a 12th-order predictor–corrector Adams method.

In Figure 9, we depict a typical phase portrait (downward displacement *versus* downward velocity of the bridge) for the free and undamped case, using parameter values consistent with those of Table 2, namely, $k = 1000$ and $W = 1000$, and for four different initial conditions. The two inner preloaded orbits shown are harmonic small-amplitude oscillations encircling the stable equilibrium point located at $y = y_0 = W/(k + 1)$ and $\dot{y} = 0$. Large amplitude bridge oscillations, on the other hand, are closed curves formed by arcs of ellipses for $y > 0$ smoothly joined to arcs of circles for $y < 0$.

Comparing our results, valid for real bridges, with those obtained in previous works [11, 14, 15], we see that the results are qualitatively similar, but with widely different numerical values. The actual elasticity constant is about a hundred times higher, and the actual preload a thousand times higher than in previous analyses. This causes an enhancement of the nonlinearity effects on real bridges, characterized by a pronounced asymmetry of the effective potential and on the arcs of ellipses in the phase space trajectories for positive deflections. Was this effect to be isolately applied, the equilibrium point y_0 would practically coincide with the origin, ruling out preloaded orbits. However, actual bridges also have strong preloading, and this brings about the preloaded orbits again, as shown in Figure 9.

Now we look at forced and undamped vibrations, for which the values of excitation frequency and amplitude for actual bridges, with respect to those used in previous works, are 10^1 and 10^2 times higher,

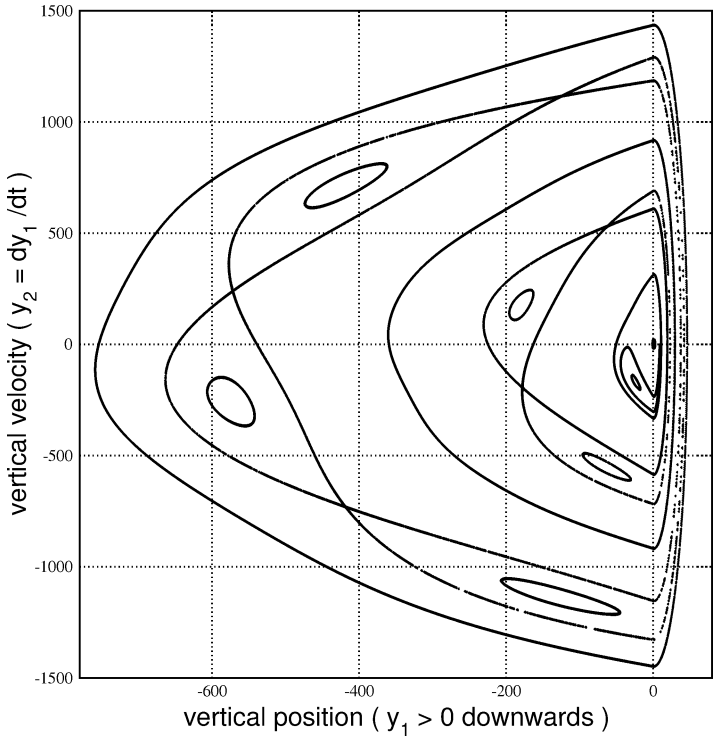

Figure 10. Trajectories in the phase plane ($y_1 = y$, $y_2 = \dot{y}$) for the Poincaré map of the undamped and forced bridge oscillations, with $B = 100$, $\omega = 10$, $k = 1000$, and $W = 1000$, corresponding to different initial conditions.

respectively. A typical phase portrait depicting such a situation is shown in Figure 10. It depicts the scenario expected for quasi-integrable Hamiltonian systems. The unforced and undamped system was a one-degree of freedom Hamiltonian system, where the canonically conjugated variables were the downward displacement and its time rate. The addition of a time-periodic perturbation term makes the system behave like a one and a half-degree of freedom Hamiltonian system. In this case, it is no longer integrable since it lacks a second constant of motion [14].

If the excitation amplitude is small, however, we can treat the system as being quasi-integrable, what enables us to use some powerful results from Hamiltonian dynamics, such as canonical perturbation theory and KAM theory, to qualitatively predict what is happening [27]. The key factor to predict the behavior of the undamped and unforced bridge, when perturbed by a term which destroys integrability, is the winding number, or the ratio between the natural frequency of the bridge and the frequency of the wind-induced excitation. If the winding number is a rational number of the form m/n, with m and n co-prime integers, we have a m:n resonance.

In terms of the Poincaré surface of section [Figure 10], we have m distinct points for the trajectory in the center of a m:n resonance. These are marginally stable periodic orbits for the time-T map, whose eigenvalues are equal to one in absolute value. These periodic orbits are encircled by nested curves in a pendular shape, or Poincaré–Birkhoff islands [27]. On the other hand, if the winding number is an irrational number, the trajectory never closes on itself, and densely fills a torus, represented by closed curves in the Poincaré section (quasi-periodic response).

The example depicted in Figure 10 exhibits a 1:1 primary resonance (harmonic) located close to the preloaded equilibrium point of the unforced system, as well as resonances with m equal to 2 and 3

(sub-harmonics), in increasing order of relative distance to the 1:1 central resonance. The outermost closed curve shown in Figure 10 represents a quasi-periodic orbit, just like the closed curves encircling the resonances. Although the Poincaré–Birkhoff islands have pendular shapes, their separatrices actually do not join together smoothly. When the system is not integrable, the separatrices intercept each other in an infinite number of homoclinic and heteroclinic points, giving rise to a chaotic dynamics, but limited to a thin area-filling layer surrounding the island's borders [27]. The width of these layers is proportional to the perturbation strength. In fact, in Figure 10, these chaotic layers do exist but are too narrow to be observed at this resolution. KAM theory predicts that most non-chaotic trajectories are quasi-periodic: under a sufficiently small perturbation most irrational tori are preserved, even though with some alteration of their shapes.

6. Multi-Stability in the Damped Bridge Dynamics

We consider the effects of adding a small viscous damping in the otherwise conservative system represented by the suspension bridge model. The discussion is based on the properties the system displays in the absence of dissipation, and are related to the periodic, quasi-periodic or chaotic nature of the orbits. Being now a dissipative system, there is no longer an energy surface to work with, but as the system still have a time-periodic variable related to the external forcing, we can also make a Poincaré section by a stroboscopic, or time-T sampling: $(y(t), \dot{y}(t)) \mapsto f_{\mathrm{T}}(y, \dot{y}) = (y(t+T), \dot{y}(t+T))$.

The damping parameter we estimated for real bridges is about 10 times the value used in previous numerical simulations [11, 14, 15]. The phase portraits are very sensitive to the introduction of damping, and this difference of just one order of magnitude is sufficient to change the dynamics in a rather drastic way. In order to make this evident, we first consider the case of a bridge with a very small damping coefficient ($\alpha = 0.01$, one order of magnitude smaller than for real bridges). The corresponding stroboscopic plot is shown in Figure 11. The regions with different shades of gray represent basins of attraction of different attractors of the dissipative system, or the sets of initial conditions which

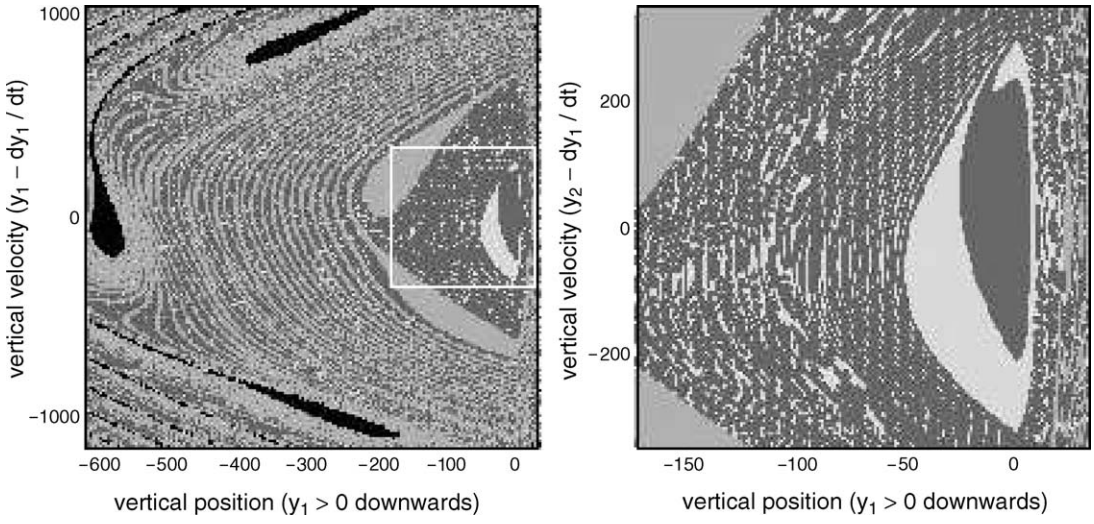

Figure 11. Left panel: phase portrait ($y - \dot{y}$) for the stroboscopic (time-T) map for $W = 1000$, $\delta = 0.01$, $k = 1000$, $B = 100$, and $\omega = 2\pi/T = 10$. The basins of attraction of period-N orbits are depicted in white (period-1); dark gray (a coexisting period-1); light gray (period-2); and black (period-3). Right panel: magnification of a portion of the phase portrait.

asymptote to these attractors. The shades of gray identify the basins of the two coexisting attractors with periods equal to 1 (white and dark gray), and two other attractors with periods 2 (light gray) and 3 (black). Orbits with higher periods may exist, but their basins would be too small to be numerically resolved.

Figure 11 illustrates multi-stability, or the existence of, at least, three basins of attractions corresponding to asymptotically periodic orbits corresponding to sub-harmonics of the periodic driving term. The general features shown in Figure 11 are expected for conservative systems with small dissipation, and can be explained in rather general grounds. The island centers, which were marginally stable periodic orbits (centers) of the conservative system, become periodic attractors (sinks or stable foci) for the stroboscopic map, whose eigenvalues are smaller than one in absolute value [28]. The periodic orbits in Figure 11a are labeled $p1a$, $p1b$, $p2$, and $p3$. While, in the Hamiltonian case, there is an infinite number of periodic orbits, we find only a finite number of attractors in the weakly dissipative system for a fixed damping, their number decaying as the damping coefficient increases from zero [29].

With dissipation, the invariant curves inside a Poincaré–Birkhoff island are entirely destroyed (since there is no longer an energy surface), and the region they occupied in the Poincaré section becomes roughly the basin of attraction of the stable focus corresponding to that period. The chaotic orbits of the conservative system become chaotic transients in the weakly dissipative case, eventually asymptoting to some of the coexisting attractors [30]. The set of points that do not asymptote to any of the sinks has Lebesgue measure zero and includes points on the boundaries of the basins of different sinks [29]. It has been numerically observed that attractors of high periods have comparatively small basins of attraction, hence they are somewhat difficult to detect [29]. Chaotic attractors also follow this rule and they are found only very rarely in weakly dissipative systems, for their basins are extremely small. In spite of this, chaotic dynamics may be present for trajectories restricted to fractal basin boundaries, and results in long chaotic transients for trajectories near the boundaries [30].

A magnification of a portion of this phase portrait is in the right panel of Figure 11, where it is apparently a very intricate structure for the basins of attraction, since the boundary basins present a highly incursive and convoluted nature. The most evident part of each basin is formed by the lobes reminiscent from the corresponding Poincaré–Birkhoff islands of the conservative limit. Due to the time-periodic nature of the perturbation, these lobes develop striations which spiral around the former equilibrium point in a very intricate manner. The basin striations accumulate at a logarithmic rate and makes the striated structure as we move far from the center of the figure. It must be stressed that the basin boundary is not a fractal, although it may give the false visual impression of being such. Even a calculation of the box-counting basin boundary dimension through the uncertainty exponent technique would give a misleading fractal result [14]. In fact, the basin boundary is rigorously a smooth non-fractal curve which simply spirals with a logarithmic accumulation of basin bands.

The mechanism underlying this *band accumulation* process, can be understood by analyzing the basin boundary between the basins of two attractors in Figure 11. Let us consider a segment of the basin boundary, or a *partitioning line* (Figure 12). There is an unstable saddle orbit belonging to the basin boundary, which is the closure of the stable manifold of the saddle. Since the time-T map is invertible by construction, we compute the forward and backward image sets in the phase plane. Under the backward iteration of the map, the images of some set A of points intersecting this unstable manifold, or $f^{-n}(A)$, approach the saddle as $n \to \infty$.

Let the set A be part of one of the basin bands in Figure 11, represented by the boundary line. The image of this boundary line under the backward dynamics of the map f_{T} is supposed to cross the unstable manifold of the saddle. The backward images of this boundary approach the saddle as time increases in such a way that: (i) the intersection points between the unstable manifold and the

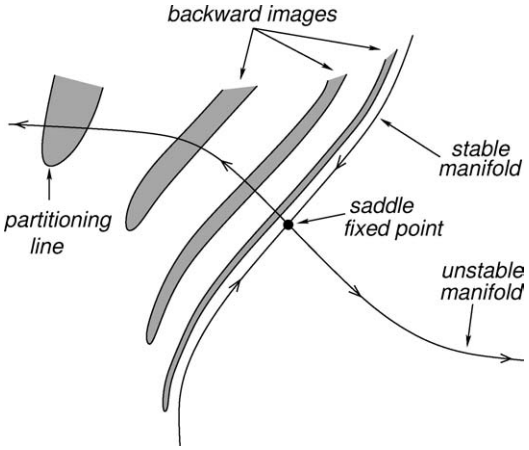

Figure 12. Logarithmic accumulation of basin bands towards the stable manifold of a saddle fixed point.

boundary of the set A converge exponentially fast, according to the corresponding unstable eigenvalue of the linearized map at the saddle; (ii) the lengths of the lobes increase exponentially to compensate for the decrease in the lobes' widths, and the lobes themselves tend to follow the stable manifold of the saddle point [31, 32]. The union of all images of the boundary is a curve which oscillates as it approaches the unstable fixed point. The net effect is that segments of the boundary line will become extremely thin filaments accumulating on the stable manifold of the saddle [33] but does not result in a fractal basin boundary. Its closure contains the stable manifold.

It must be noted, however, that even when the basin boundary is a smooth, yet a very involved curve, this has practical implications, since a small uncertainty in the determination of the initial conditions, represented in the phase space by a circle, may intercept many bands belonging to different basins. In this case, we cannot say with certainty to what attractor the trajectory starting somewhere inside this circle will asymptote to. Moreover, if noise is added to such a system (we can think of the random fluctuations of the wind velocity, for example), it may also happen that a trajectory lying in some basin hops to another basin, and so on [34]. This phenomenon of *basin hopping* can be even more dangerous for a suspension bridge than the chaotic behavior itself, since if the attractors correspond to roadbed oscillations with a widely different amplitude, basin hopping would result in a sudden jump that may cause partial or total damage of the structure.

Now let us consider the structure of the basins of attraction when the full set of parameters for real bridges is taken into account. An example is depicted in Figure 13, where the damping has been raised to $\delta = 0.1$. We see that the fine structure present in the weak dissipation case are somewhat 'washed out', when the damping is increased, since there are now just two basins of two different period-1 attractors. These two coexisting attractors are shown separately in Figure 14, both for the continuous trajectories in the phase plane as well as the discrete points of the time-T stroboscopic mapping.

As a general pattern, in multi-stable systems the number of coexisting attractors, either periodic or chaotic, decreases as the damping coefficient is augmented. We depict in Figure 15 the coexisting periodic orbits by plotting the y-coordinate (of the stroboscopic map) *versus* dissipation coefficient δ for a fixed value of the forcing amplitude, and parameters taken from Table 2, typical of real bridges. For values of δ less than 0.04, we observe orbits with periods up to 3. As δ increases, the orbits of higher period suddenly disappear at well-defined values of the damping coefficient, until there remains only

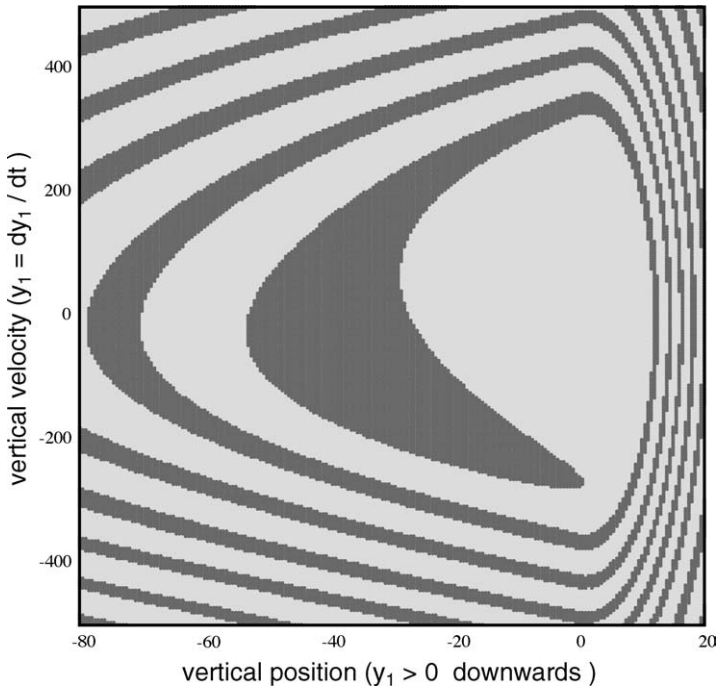

Figure 13. Phase portrait ($y - \dot{y}$) for the stroboscopic (time-T) map for the same parameters as in Table 2 with basins of attraction depicted in different shades of gray.

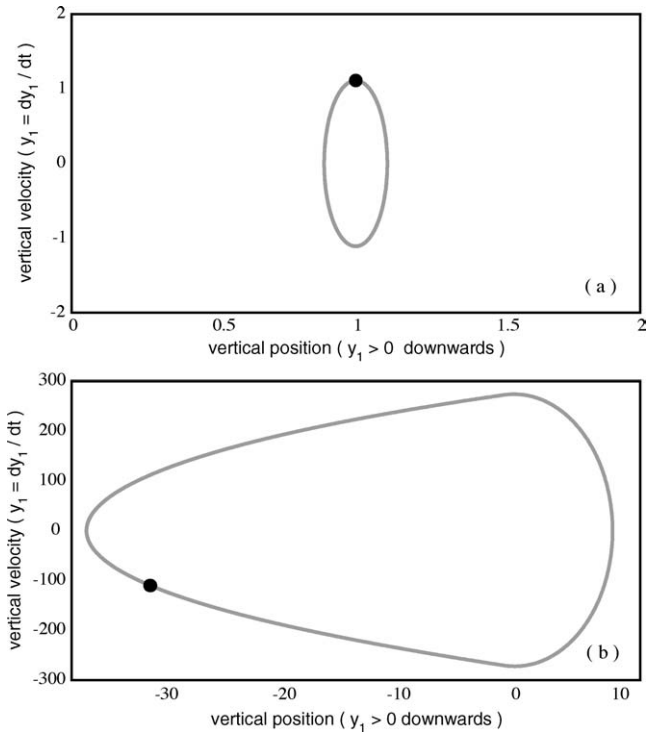

Figure 14. Trajectories in the phase plane (y, $\dot{y}$) for for the same parameters as in Table 2 and two coexisting period-1 orbits. The marked points refer to the corresponding stroboscopic map.

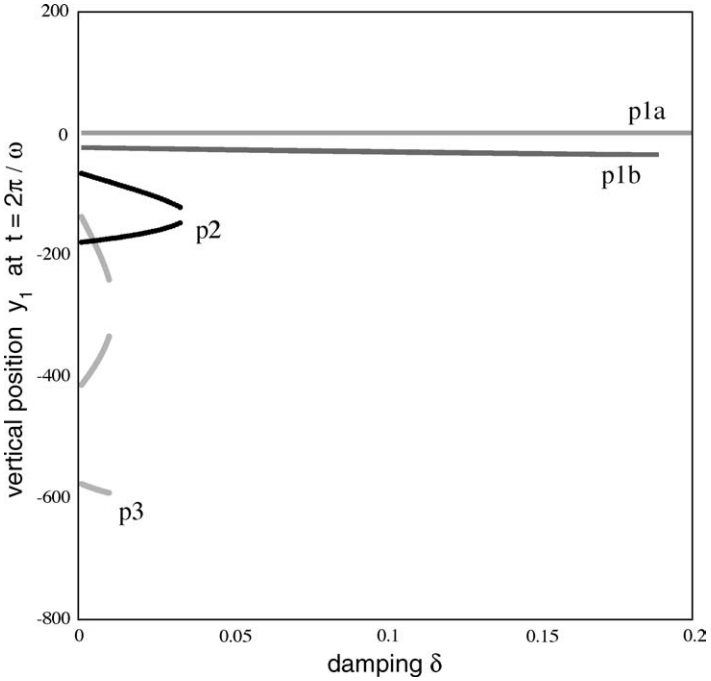

Figure 15. Bifurcation diagram for the stroboscopic map, showing the vertical position $y(t = nT)$ at discrete times *versus* the damping coefficient δ. The remaining parameters are the same as in Figure 11. Coexisting period-N orbits are indicated as pN in the figure.

the period-1 attractors for strongly damped case, for which there is a simple entrainment between the wind-induced excitation and the bridge oscillation.

7. Conclusions

In this paper, we revisited the model of suspension bridge oscillations induced by time-periodic forcing due to a von Kármán vortex street, proposed by Lazer and McKeena [3]. A single important mode; namely, the lowest vertical vibration mode, is considered from the point of view of its time dynamics. We aimed at numerical simulations using parameters estimated from suspension bridges for which they are readily available, in such a way that one can make realistic predictions about the behavior under normal and abnormal wind conditions.

The nonlinear nature of the one-sided springs, modeling the hingers, which couple the roadbed to the main suspension cable leads, in principle, to a wide variety of dynamical phenomena. In particular, it turns out that the nonlinearity of the hangers, the preload, and the amplitude excitation have been underestimated in previous numerical simulations [11, 14, 15], being two, three and two orders of magnitude higher in real bridges, respectively. A less pronounced difference has been observed in the values of the excitation frequency and the damping coefficient, which are both 10 times higher than the values used previously.

We have done numerical simulations with a realistically estimated set of parameters and found that the main factor to be taken into account is the increase of the damping effect. While in the weakly dissipative case, a very rich dynamical behavior was found [14], including chaotic behavior, when the dissipation increases , the multi-stability, while still present in the system dynamics, is significantly

less pronounced. We have observed the existence of a small number of low-period periodic orbits. In practice, just two coexisting period-1 orbits are expected to be observed, corresponding to bridge deflections with widely different amplitudes (differing by two orders of magnitude). Considering the presence of environmental noise, we would expect noise-induced jumps in phase space, when the initial conditions are close enough to the basin boundaries. Taking into account the large difference of amplitudes corresponding to these two possible coexisting periodic states, under the action of noise a trajectory may hop from one basin to another, causing potentially dangerous large amplitude jumps which can make the bridge collapse.

Although our analysis has been limited to just one vibrational mode, we expect similar features for the higher vibrational, as well as torsional and other combined modes. However, further work is still needed to investigate the role of basin hopping in situations where the coexisting behaviors represent oscillations which are not necessarily as close as in our estimations.

Acknowledgements

This work was made possible by partial financial support from CNPq and FAPESP (Brazilian Government Agencies).

References

1. Amann, O. H., von Kármán, T., and Woodruff, G. B., *The Failure of the Tacoma Narrows Bridge*, Federal Works Agency, Washington, 1941.
2. Billah, K. Y. and Scanlan, R. H., 'Resonance, Tacoma Narrows bridge failure, and undergraduate physics textbooks', *American Journal of Physics* **59**, 1991, 118–124.
3. Lazer, A. C. and McKenna, P. J., 'Large amplitude periodic oscillations in suspension bridges: Some new connections with nonlinear analysis', *SIAM Review* **58**, 1990, 537–578.
4. Nayfeh, A. H. and Mook, D. T., *Nonlinear Oscillations*, Wiley-Interscience, New York, 1979.
5. Aidanpaa, J. O., Shen, H. H., and Gupta, R. B., 'Stability and bifurcations of a stationary state for an impact oscillator', *Chaos* **4**, 1994, 621–630.
6. Wiercigroch, M. and DeKraker, B., *Applied Nonlinear Dynamics and Chaos of Mechanical Systems with Discontinuities*, World Scientific, Singapore, 2000.
7. Wiercigroch, M., 'Modelling of dynamical systems with motion dependent discontinuities', *Chaos, Solitons and Fractals* **11**, 2000, 2429–2442.
8. Jerrelind, J. and Stensson, A., 'Nonlinear dynamics of parts in engineering systems', *Chaos, Solitons and Fractals* **11**, 2000, 2413–2418.
9. Heertjes, M. F. and Van De Molengraft, M. J. G., 'Controlling the nonlinear dynamics of a beam system', *Chaos, Solitons and Fractals* **12**, 2001, 49–66.
10. http://www.vibrationdata.com/Tacoma.htm.
11. Doole, S. H. and Hogan, S. J., 'A piecewise linear suspension bridge model: Nonlinear dynamics and orbit continuation', *Dynamics and Stability of Systems* **11**, 1996, 19–47.
12. Doole, S. H. and Hogan, S. J., 'Nonlinear dynamics of the extended Lazer-McKenna bridge oscillation model', *Dynamics and Stability of Systems* **15**, 2000, 43–58.
13. Zavodney, L. D., Nayfeh, A. H., and Sanchez, N. E., 'Bifurcations and chaos in parametrically excited single-degree-of-freedom systems', *Nonlinear Dynamics* **1**, 1990, 1–21.
14. Freitas, M. S. T. de, Viana, R. L., and Grebogi, C., 'Multistability, basin boundary structure, and chaotic behavior in a suspension bridge model', *International Journal of Bifurcation and Chaos* **14**, 2004, 927–950.
15. Freitas, M. S. T. de, Viana, R. L., and Grebogi, C., 'Erosion of the safe basin for the transversal oscillations of a suspension bridge', *Chaos, Solitons and Fractals* **18**, 2003, 829–841.
16. Hartog, D. and Pieter, J., *Advanced Strength of Materials*, Dover, New York, 1987.
17. Blevins, R. D., *Flow-Induced Vibration*, VanNostrand Reinhold, New York, 1997.
18. Shaw, S. W. and Holmes, P. J., 'A periodically forced piecewise linear oscillator', *Journal of Sound and Vibration* **90**, 1983, 129–155.

19. Thompson, J. M. T., Bokaian, A. R., and Ghaffari, R., 'Subharmonic resonances and chaotic motions of a bilinear oscillator', *I.M.A. Journal of Applied Mathematics* **31**, 1983, 207–234.
20. Whiston, G. S., 'The vibro-impact response of a harmonically excited and preloaded one-dimensional linear oscillator', *Journal of Sound and Vibration* **115**, 1987, 303–319.
21. Cao, Q., Xu, L., Djidjeli, K., Price, W. G., and Twizell, E. H., 'Analysis of period-doubling and chaos of a non-symmetric oscillator with piecewise linearity', *Chaos, Solitons and Fractals* **12**, 2001, 1917–1927.
22. O'Connor, C., *Design of Bridge Superstructures*, Wiley, New York, 1971.
23. Daugherty, R. L. and Ingersoll, A. C., *Fluid Dynamics with Engineering Applications*, 5th edn., McGraw Hill, New York, 1954.
24. Shames, I. H., *Mechanics of Fluids*, 2nd edn., McGraw Hill, New York, 1982.
25. Thompson, J. M. T., *Instabilities and Catastrophes in Science and Engineering*, Wiley, New York, 1982.
26. Morgenthal, G., 'Comparison of Numerical Methods for Bridge-Deck Aerodynamics', M. Phil. Thesis, Cambridge University, Cambridge, UK, 2000.
27. Lichtenberg, A. J. and Lieberman, M. A., *Regular and Chaotic Dynamics*, 2nd edn., Springer, New York, 1997.
28. Feudel, U., Grebogi, C., Hunt, B. R., and Yorke, J. A., 'Map with more than 100 coexisting low-period periodic attractors,' *Physical Review E* **54**, 1996, 71–81.
29. Feudel, U. and Grebogi, C., 'Multistability and the control of complexity', *Chaos* **7**, 1997, 597–604.
30. Feudel, U., Grebogi, C., Poon, L., and Yorke, J. A., 'Dynamical properties of a simple mechanical system with a large number of coexisting periodic attractors', *Chaos, Solitons and Fractals* **9**, 1998, 171–180.
31. McDonald, S. W., Grebogi, C., Ott, E., and Yorke, J. A., 'Final state sensitivity: An obstruction to predictability', *Physics Letters A* **99**, 1983, 415–418.
32. McDonald, S. W., Grebogi, C., Ott, E., and Yorke, J. A., 'Fractal basin boundaries', *Physica D* **17**, 1985, 125–153.
33. Pentek, A., Toroczkai, Z., Tel, T., Grebogi, C., and Yorke, J. A., 'Fractal boundaries in open hydrodynamical flows: Signatures of chaotic saddles', *Physical Review E* **51**, 1995, 4076–4088.
34. Kraut, S., Feudel, U., and Grebogi, C., 'Preference of attractors in noisy multistable systems', *Physical Review E* **59**, 1999, 5253–5260.